

Increasing Quantum Limited Sensitivity of  
Interferometers Using Electromagnetically Induced  
Transparency

Hunter Rew

Advised by Dr. Eugeny E. Mikhailov

May 4, 2016

## **Abstract**

We explore the properties of electromagnetically induced transparency (EIT) and its applications as a frequency filter in the field of gravitational wave interferometry. Through modeling and simulation, we determine parameters for atom-light configurations of multi-state atoms which will theoretically allow for transmission frequencies and intensities of squeezed light in a range suitable for increasing sensitivity levels in gravitational wave interferometers. This corresponds to contrasts greater than 50% and linewidths of 100 Hz or less. We produce EIT experimentally and characterize the distributions by fitting them to a generalized Lorentzian. The largest contrast observed is 3.9% with a linewidth of 660 Hz. The smallest linewidth observed is 260 Hz with a contrast of 0.42%.

# Contents

<b>1</b>	<b>Introduction</b>	<b>3</b>
1.1	Gravitational wave interferometers . . . . .	3
1.2	Squeezed states and their application to interferometry . . . . .	4
1.3	Electromagnetically induced transparency as a frequency filter . . . . .	5
<b>2</b>	<b>Theory</b>	<b>6</b>
2.1	The dark state in a 3-state atom . . . . .	6
2.2	The lambda model . . . . .	8
<b>3</b>	<b>Simulation</b>	<b>11</b>
3.1	Simulation methods and parameters . . . . .	11
3.2	Simulation results and analysis . . . . .	12
<b>4</b>	<b>Experiment</b>	<b>18</b>
4.1	Experimental setup and procedures . . . . .	18
4.1.1	Setup . . . . .	18
4.1.2	Procedures for varying beam intensity . . . . .	19
4.1.3	Procedures for varying cell density . . . . .	19
4.1.4	Procedures for varying beam waist . . . . .	20
4.2	Experimental data and data analysis . . . . .	20
4.2.1	Processing of raw data . . . . .	20
4.2.2	Contrast and linewidth vs power for varying particle concentration . . . . .	22
4.2.3	Contrast and linewidth vs intensity for varying beam waist . . . . .	22
4.3	Error analysis . . . . .	27
<b>5</b>	<b>Conclusions</b>	<b>28</b>
<b>6</b>	<b>References</b>	<b>29</b>

# List of Figures

1.1	The Laser Interferometer Gravitational Wave Observatory . . . . .	3
1.2	Squeezed uncertainty in the phase and momentum quadratures. . . . .	5
2.1	2 state configuration with a field applied at the transition between the ground state and excited state. . . . .	6
2.2	3 state configuration with 2 fields applied at the transitions between the ground states and excited state. . . . .	8
2.3	The $\Lambda$ configuration. . . . .	10
3.1	An example EIT transmission distribution. . . . .	12
3.2	The evolution of EIT as it propagates through an atomic medium. . . . .	13
3.3	Transmission vs drive intensity and medium length. . . . .	14
3.4	Contrast vs drive intensity and medium length. . . . .	15
3.5	Linewidth vs drive intensity and medium length. . . . .	16
3.6	Transmission vs drive intensity and medium length for the intersection of desirable contrasts and linewidths. . . . .	17
4.1	A diagram of the experiment configuration. . . . .	18
4.2	Fit of experimental EIT . . . . .	21
4.3	Contrast vs power for varying particle concentration . . . . .	23
4.4	Linewidth vs power for varying particle concentration . . . . .	24
4.5	Contrast vs intensity for varying beam waist . . . . .	25
4.6	Width vs power for varying beam waist . . . . .	26

# Introduction

## 1.1 Gravitational wave interferometers

A prediction of the general theory of relativity is that moving objects produce waves in spacetime which propagate in all directions at the speed of light. These gravitational waves (GWs) contract space in one dimension while expanding space in transverse dimensions, alternating with each half period. Attempts to confirm the existence of GWs have resulted in the construction of high precision laser interferometers across the Earth [1]. These interferometers use mirrors as test masses so that as a GW passes through, one arm will shorten while the other elongates, causing a measurable phase shift of the light. A diagram of one of these interferometers is shown in Figure 1.1.

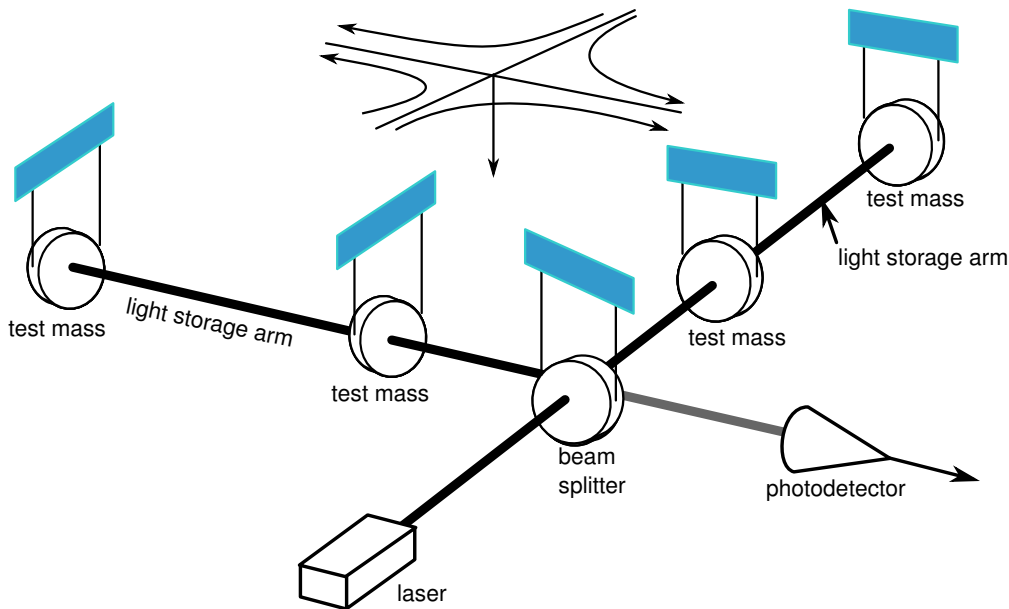


Figure 1.1: The Laser Interferometer Gravitational Wave Observatory (LIGO) is a Michelson interferometer with 4 km long Fabry-Perot cavities as arms. LIGO has 2 sites 3000 km apart in Livingston, Louisiana and Hanford, Washington.

## 1.2 Squeezed states and their application to interferometry

The uncertainty principle places a fundamental limit on how precisely two quadratures, such as position and momentum, can be known. A generic form of this limit is shown in Equation 1.1, where  $\chi_1$  and  $\chi_2$  are the measurable quadratures.

$$\Delta\chi_1\Delta\chi_2 \geq Limit \tag{1.1}$$

Due to the Heisenberg uncertainty principle, the amplitude and phase of light cannot be known beyond a quantum limited precision. This uncertainty in a measurement can be visualized as Figure 1.2, where rather than a distinct point measurement, there is a "ball" of uncertainty in the phase-amplitude plane. The area of this ball is governed by the uncertainty principle, however, there is no law that these uncertainties must be symmetric [1]. For example, the ball could be squeezed into an ellipse at some angle (as shown in Figure 1.2) so that, while maintaining the same total area, the uncertainty in amplitude becomes much larger than the uncertainty in phase. This is analogous to purposefully losing information of the amplitude (increasing its uncertainty), so that the phase can be known with greater precision while still satisfying the uncertainty principle. Once this is done the light is said to be in a squeezed state. Using squeezed light, an interferometer can measure the signal of interest beyond the quantum limit, thereby increasing sensitivity to GWs [1]. This would enable observatories such as LIGO to make detections more frequently from a broader range of astronomical sources. However, LIGO's optical fields are already in a squeezed state due to radiation pressure noise within the Fabry-Perot cavities [2]. In order to inject a new squeezed state, the squeeze angle must be matched [1,2] This necessitates the use of an optical filter with a linewidth  $< 100$  Hz [1,2].

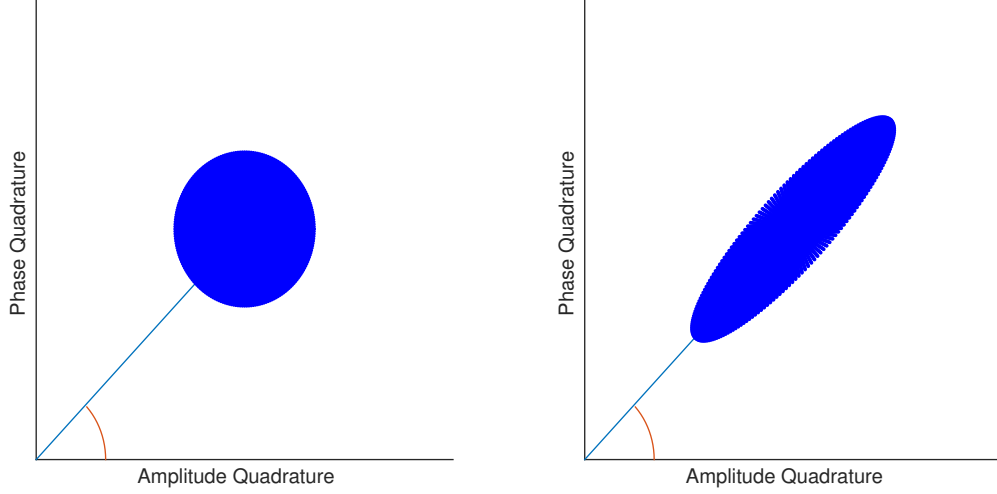


Figure 1.2: The left plot shows a symmetric "ball" of uncertainty. The right plot shows the uncertainty squeezed.

### 1.3 Electromagnetically induced transparency as a frequency filter

Electromagnetically Induced Transparency (EIT) is the phenomenon of an opaque material becoming transparent for certain frequencies of light. This occurs by "pumping" atoms into a "dark" state by applying optical fields which match the frequency difference between excited states and the hyperfine ground states, creating a superposition of the ground states which doesn't interact with the applied fields [3]. This allows a "probe" to pass through the medium with high transmission across a slim range of frequencies. An EIT media could potentially be used as a filter for rotating the angle of an injected squeezed state, while maintaining low optical losses [2].

# Theory

## 2.1 The dark state in a 3-state atom

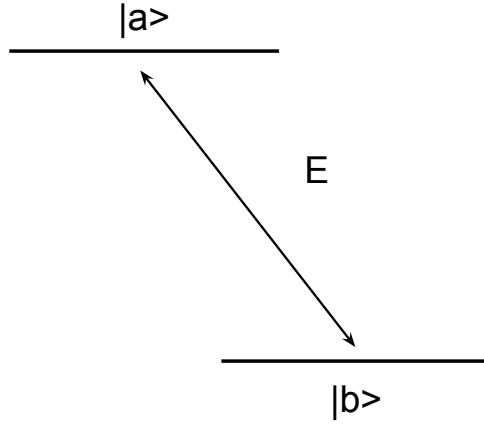


Figure 2.1: 2 state configuration with a field applied at the transition between the ground state and excited state.

In order for EIT to be realized, there must be a state for a 3 level atom in which absorption and spontaneous emission do not occur. To prove that this is possible, one must show that the population of the excited state can be zero. For simplicity, we will begin with a simplified 2 level structure, then expand the solution to 3 levels. Consider the wave function of the configuration shown in Figure 2.1. This is a 2 level atomic structure, with ground state  $|b\rangle$ , excited state  $|a\rangle$ , and a field  $E$  applied at the transition frequency.

$$\Psi(t) = C_a(t)e^{-i\omega_a t} |a\rangle + C_b(t)e^{-i\omega_b t} |b\rangle \quad (2.1)$$

Here  $C_a$  and  $C_b$  are the state coefficients, where  $|C_i|^2$  is the probability of finding an atom in state  $|i\rangle$ , and  $\omega_i$  is the frequency of energy level  $i$ . We will look for a condition which forces the time derivative of  $C_a$  to be zero by taking the Hamiltonian.

$$i\hbar \frac{\partial \Psi(t)}{\partial t} = \hat{H} \Psi(t) = (\hat{H}_0 + \hat{H}') \Psi(t) \quad (2.2)$$

$$\hat{H}_0 |\Psi(t)\rangle = (\hbar\omega_a |a\rangle \langle a| + \hbar\omega_b |b\rangle \langle b|) |\Psi(t)\rangle \quad (2.3)$$

$$\hat{H}' |\Psi(t)\rangle = (\hbar\Omega e^{-i\omega t} |a\rangle \langle b| + \hbar\Omega e^{i\omega t} |b\rangle \langle a|) |\Psi(t)\rangle \quad (2.4)$$

The Hamiltonian consists of two parts, the unperturbed Hamiltonian,  $\hat{H}_0$ , and the interaction Hamiltonian,  $\hat{H}'$ .  $\Omega$  is called the Rabi frequency, and is defined as:

$$\Omega = \frac{d_{ab}\varepsilon}{\hbar} \quad (2.5)$$

where  $d_{ab}$  is the dipole moment between states  $|a\rangle$  and  $|b\rangle$  and  $\varepsilon$  is the field amplitude of E. Now, by plugging Equations 2.1, 2.3, and 2.4 into Equation 2.2, we can solve for the time derivatives of the coefficients as below:

$$i\dot{C}_a = \Omega C_b e^{-i(\omega - \omega_{ab})t} \quad (2.6)$$

$$i\dot{C}_b = \Omega C_a e^{-i(\omega - \omega_{ab})t} \quad (2.7)$$

where  $\omega_{ab} = \omega_a - \omega_b$ , and  $\omega$  is the frequency of the applied field. Now we can expand these solutions to a 3 level system. The corresponding wave function and solutions are shown in Equations 2.8 through 2.11.

$$\Psi(t) = C_a(t) e^{-i\omega_a t} |a\rangle + C_b(t) e^{-i\omega_b t} |b\rangle + C_c e^{-i\omega_c t} |c\rangle \quad (2.8)$$

$$i\dot{C}_a = \Omega_1 C_b e^{-i(\omega_1 - \omega_{ab})t} + \Omega_2 C_c e^{-i(\omega_2 - \omega_{ac})t} \quad (2.9)$$

$$i\dot{C}_b = \Omega_1 C_a e^{-i(\omega_1 - \omega_{ab})t} \quad (2.10)$$

$$i\dot{C}_c = \Omega_2 C_a e^{-i(\omega_2 - \omega_{ac})t} \quad (2.11)$$

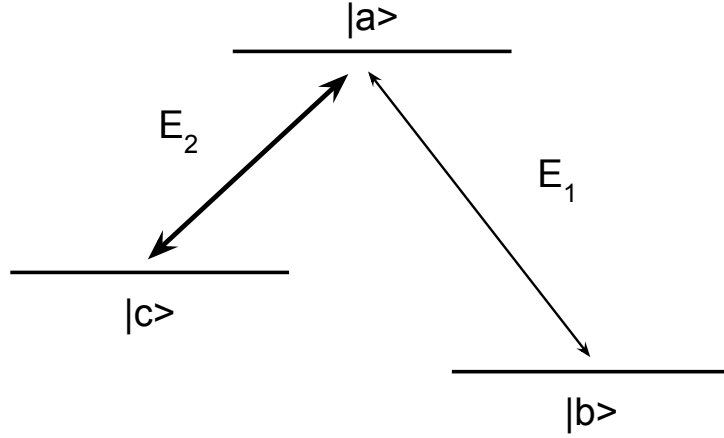


Figure 2.2: 3 state configuration with 2 fields applied at the transition between the ground states and excited state.

Setting Equation 2.9 to zero, we arrive at the condition of  $\Omega_1 C_b = -\Omega_2 C_c$  in the case of a 2 photon resonance.

$$\omega_{bc} = \omega_2 - \omega_1 \quad (2.12)$$

This is called such because the frequency difference of fields  $E_1$  and  $E_2$  is equal to the difference in transitions from the two ground states. Now by applying the conditions of  $\dot{C}_a = 0$  to Equation 2.8, we arrive at a wave function which is a superposition of only the two ground states, the dark state.

$$|D\rangle = \frac{\Omega_2 e^{-i\omega_b t} |b\rangle - \Omega_1 e^{-i\omega_c t} |c\rangle}{\sqrt{\Omega_1^2 + \Omega_2^2}} \quad (2.13)$$

## 2.2 The lambda model

The  $\Lambda$  model is a simplistic atomic configuration consisting of 3 states in total, 2 ground states and 1 excited state. A representation of the model and the optical fields that are applied is shown in Figure 2.3.  $\Omega_d$  is the drive field,  $\Omega_p$  is the probe field,  $\Delta$  is the 1-photon detuning,  $\delta$  is the 2-photon detuning,  $\gamma$  is the decay rate from the excited state,  $|a\rangle$ , to the

hyperfine ground states,  $|b\rangle$  and  $|c\rangle$ , and  $\gamma_{bc}$  is the decay rate between ground states. The population and coherence of each state is given by the derivatives of the  $3 \times 3$  density matrix with respect to time. These are reproduced below in equations 2.14 to 2.19 [4]:

$$\dot{\rho}_{aa} = -i\Omega_p^* \rho_{ab} + i\Omega_p \rho_{ba} - i\Omega_d^* \rho_{ac} + i\Omega_d \rho_{ca} - 2\gamma \rho_{aa} \quad (2.14)$$

$$\dot{\rho}_{bb} = i\Omega_p^* \rho_{ab} - i\Omega_p \rho_{ba} + \gamma \rho_{aa} - \gamma_{bc} \rho_{bb} + \gamma_{bc} \rho_{cc} \quad (2.15)$$

$$\dot{\rho}_{cc} = i\Omega_d^* \rho_{ac} - i\Omega_d \rho_{ca} + \gamma \rho_{aa} - \gamma_{bc} \rho_{cc} + \gamma_{bc} \rho_{bb} \quad (2.16)$$

$$\dot{\rho}_{ab} = -\Gamma_{ab} \rho_{ab} + i\Omega_p (\rho_{bb} - \rho_{aa}) + i\Omega_d \rho_{cb} \quad (2.17)$$

$$\dot{\rho}_{ca} = -\Gamma_{ca} \rho_{ca} + i\Omega_d^* (\rho_{aa} - \rho_{cc}) - i\Omega_p^* \rho_{cb} \quad (2.18)$$

$$\dot{\rho}_{cb} = -\Gamma_{cb} \rho_{cb} - i\Omega_p \rho_{ca} + i\Omega_d^* \rho_{ab} \quad (2.19)$$

where the coherence decay rate  $\Gamma_{ij}$  is given by [4]

$$\Gamma_{ab} = \gamma + i(\Delta + \delta) \quad (2.20)$$

$$\Gamma_{ca} = \gamma - i\Delta \quad (2.21)$$

$$\Gamma_{cb} = \gamma_{bc} + i\delta \quad (2.22)$$

Because the density matrix is Hermitian, the remaining off diagonal elements can be found as:

$$\dot{\rho}_{ij} = \dot{\rho}_{ji}^*, i \neq j \quad (2.23)$$

By tuning the drive and probe fields to match the  $|a\rangle \rightarrow |c\rangle$  and  $|a\rangle \rightarrow |b\rangle$  transitions, respectively, a coherent dark state is produced. This state deteriorates as the fields are detuned from these transitions, giving the EIT an inherent linewidth [3].

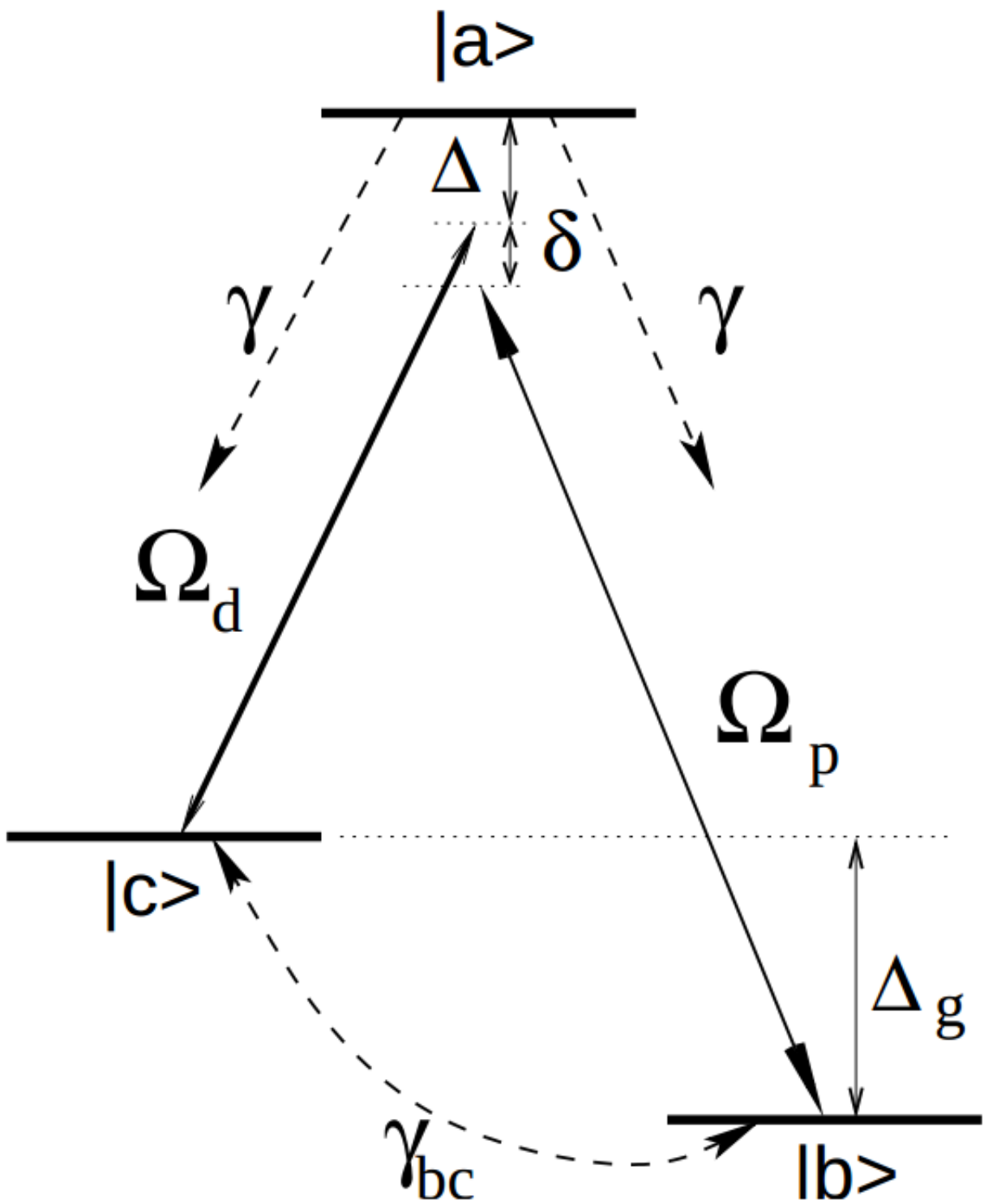


Figure 2.3:  $\Lambda$  configuration [4]

# Simulation

## 3.1 Simulation methods and parameters

In order to solve for the population of each state, we used numerical integration software called eXtensible Multi-Dimensional Simulator (XMDS). This allowed for integrating Equations 2.14 through 2.19 across time while varying the detuning to see how the dark state changed with respect to the probe frequency and propagation through a medium. Attaining high resolution in detuning and propagation quickly increases the memory requirements of the simulation, so it was necessary to utilize William and Mary's high performance computing cluster, SciClone.

Simulations were run with the following parameters:

- Drive Rabi frequency ( $\Omega_d$ ): varied from 16.6 to 25.0 KHz
- Probe Rabi frequency ( $\Omega_p$ ): 0.1 Hz
- Excited state decay ( $\gamma$ ): 6 MHz
- Ground state decay ( $\gamma_{bc}$ ): 1 Hz
- Length of medium: varied from 0 to 2 cm
- Particle density of medium:  $1 \times 10^{15}$  particles per  $\text{m}^3$

Equation 3.1 is used to account for propagation in our simulations [4], with  $k = 2\pi/\lambda$ ,  $\lambda = 794.7\text{nm}$ , and  $N$  as the number of interacting atoms.

$$\frac{\partial \varepsilon}{\partial z} + \frac{1}{c} \frac{\partial \varepsilon}{\partial t} = 2\pi i k N \sum_{i,j} d_{i,j} \tilde{\rho}_{i,j} \quad (3.1)$$

## 3.2 Simulation results and analysis

The result of any EIT from specific parameters is measured in two respects, the contrast and the linewidth. Using Figure 3.1 as a reference, the contrast is defined to be the difference between the peak and shoulder transmissions divided by the peak transmission. In this way it is normalized to a maximum of 100%. The linewidth is taken as the full width at half maximum (FWHM).

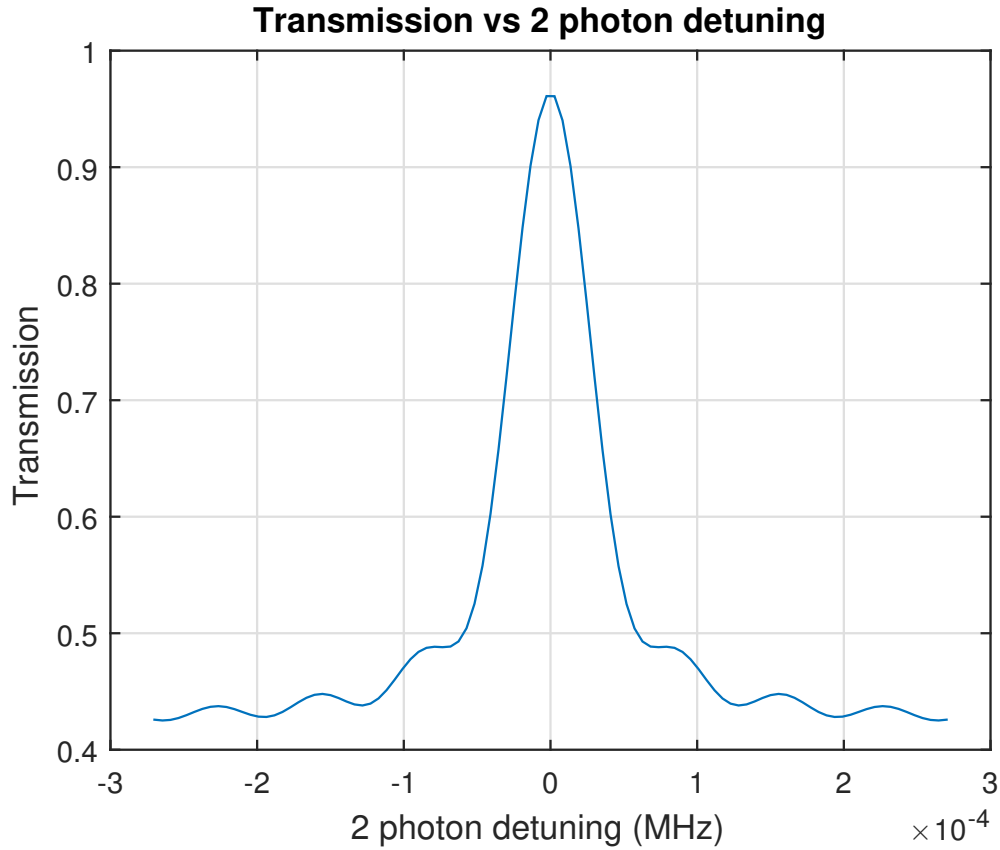


Figure 3.1: An example EIT transmission distribution.

Because the EIT does not start with precisely 100% transmission, a small percentage of the probe intensity is lost to atoms while propagating. The effects of initial drive power and propagation on transmission are shown in Figure 3.3. When the probe is detuned from the resonant frequency, however, transmission drops considerably more, resulting in the development of contrast (Figure 3.2). From Figure 3.4 one can see that contrast does

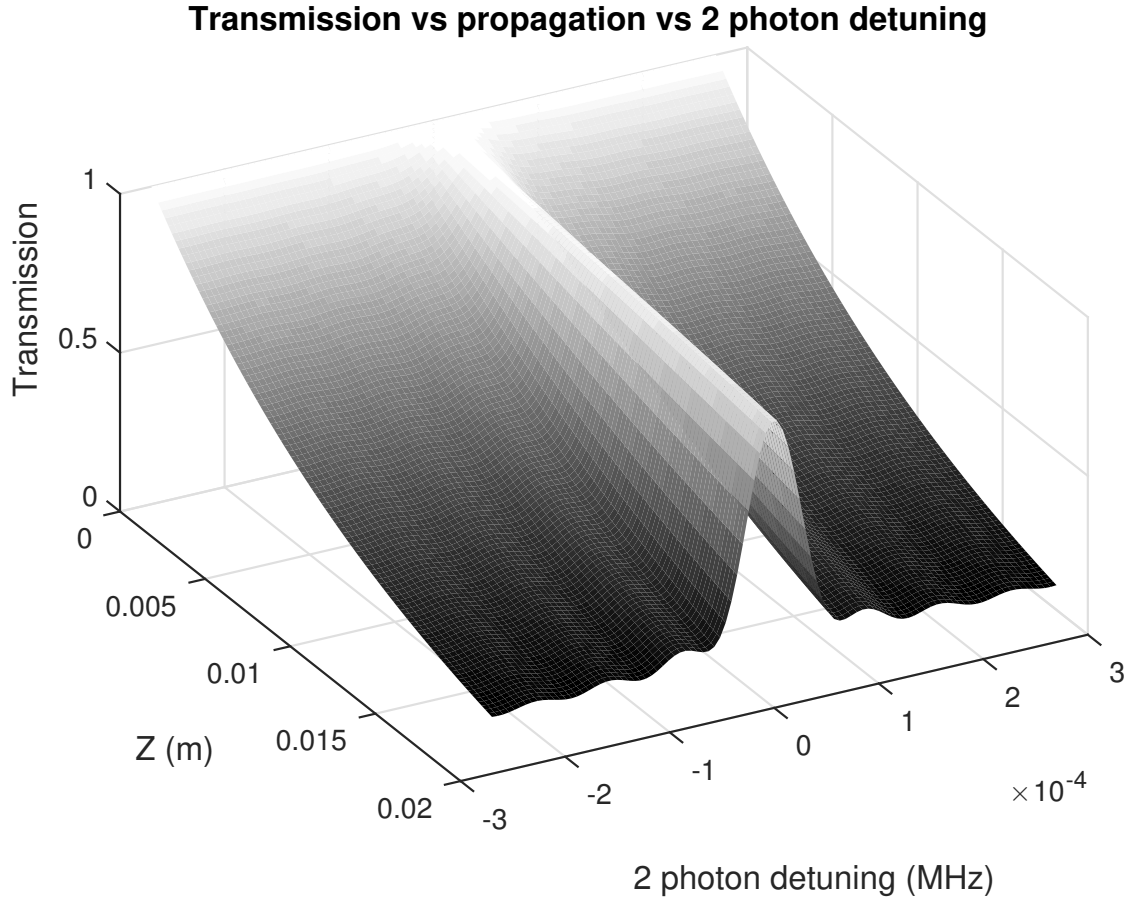


Figure 3.2: The evolution of EIT as it propagates through an atomic medium in the  $Z$  direction. With increasing atom interactions, the field is absorbed for frequencies far from resonance, while frequencies near resonance are free to pass.

indeed increase with propagation. This also results in a narrowing of the linewidth with propagation, as shown in Figure 3.5. Using Figure 3.6 we can see that the requirement of a linewidth  $< 100$  Hz can be achieved with contrast  $> 50\%$  across drives ranging from 17 kHz to at least 25 kHz for nearly any medium length greater than 1 cm. This is the range that is useful for applications of EIT as a frequency filter in gravitational wave interferometers.

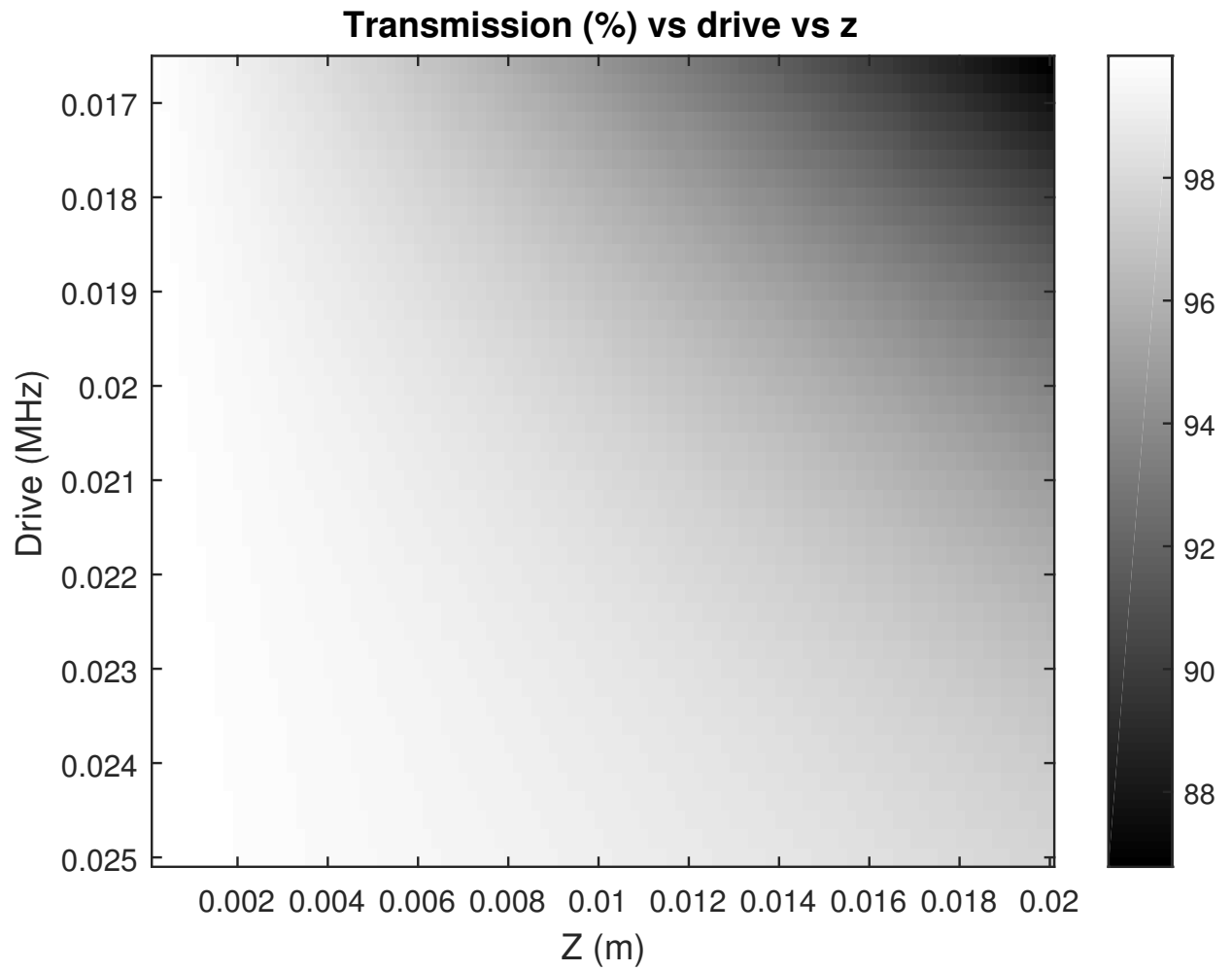


Figure 3.3: This map shows how the transmission of the EIT is affected by the Drive frequency and length ( $Z$ ) of the atomic media through which the fields are propagating.

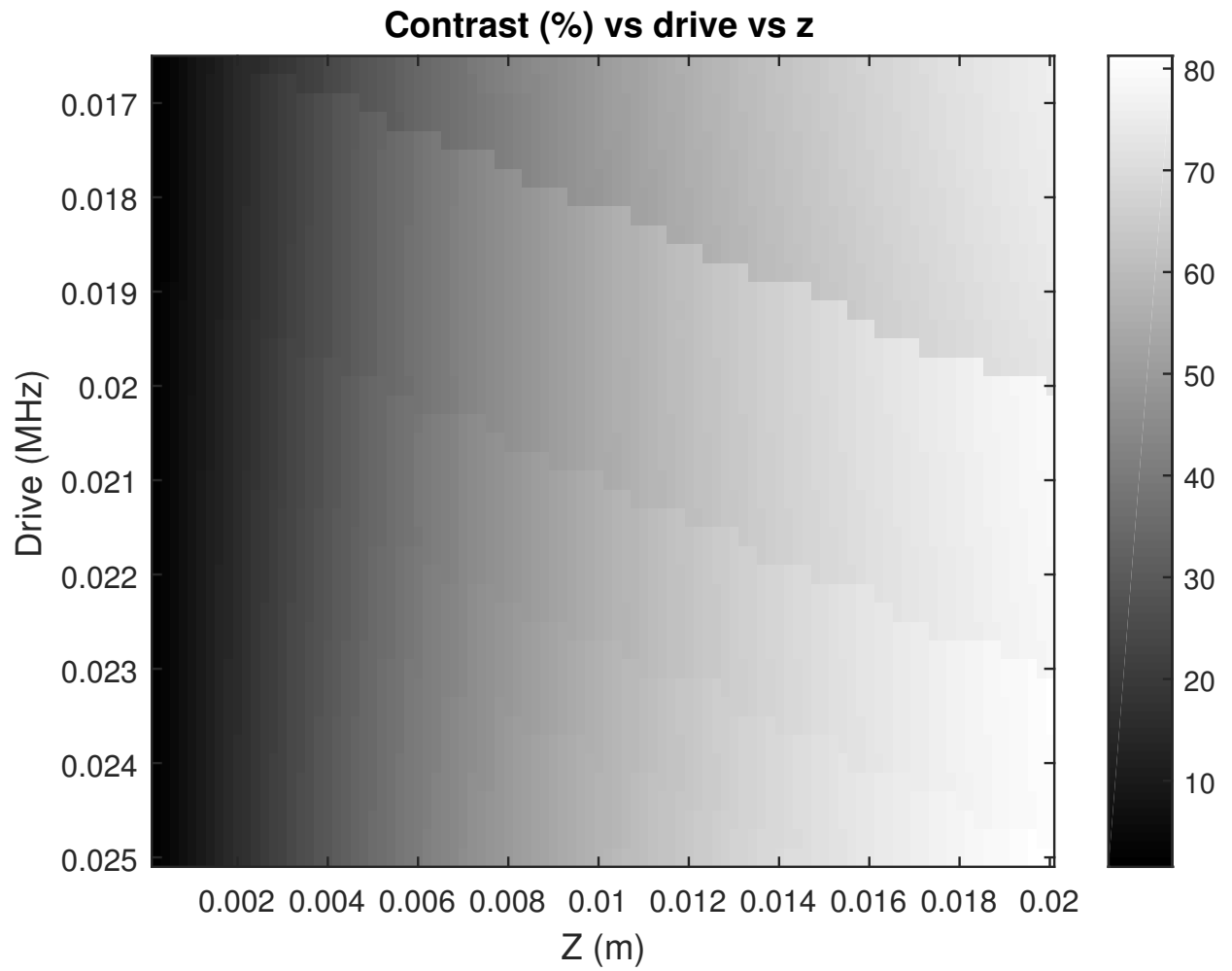


Figure 3.4: This map shows how the contrast of the EIT is affected by the Drive frequency and length ( $Z$ ) of the atomic media through which the fields are propagating.

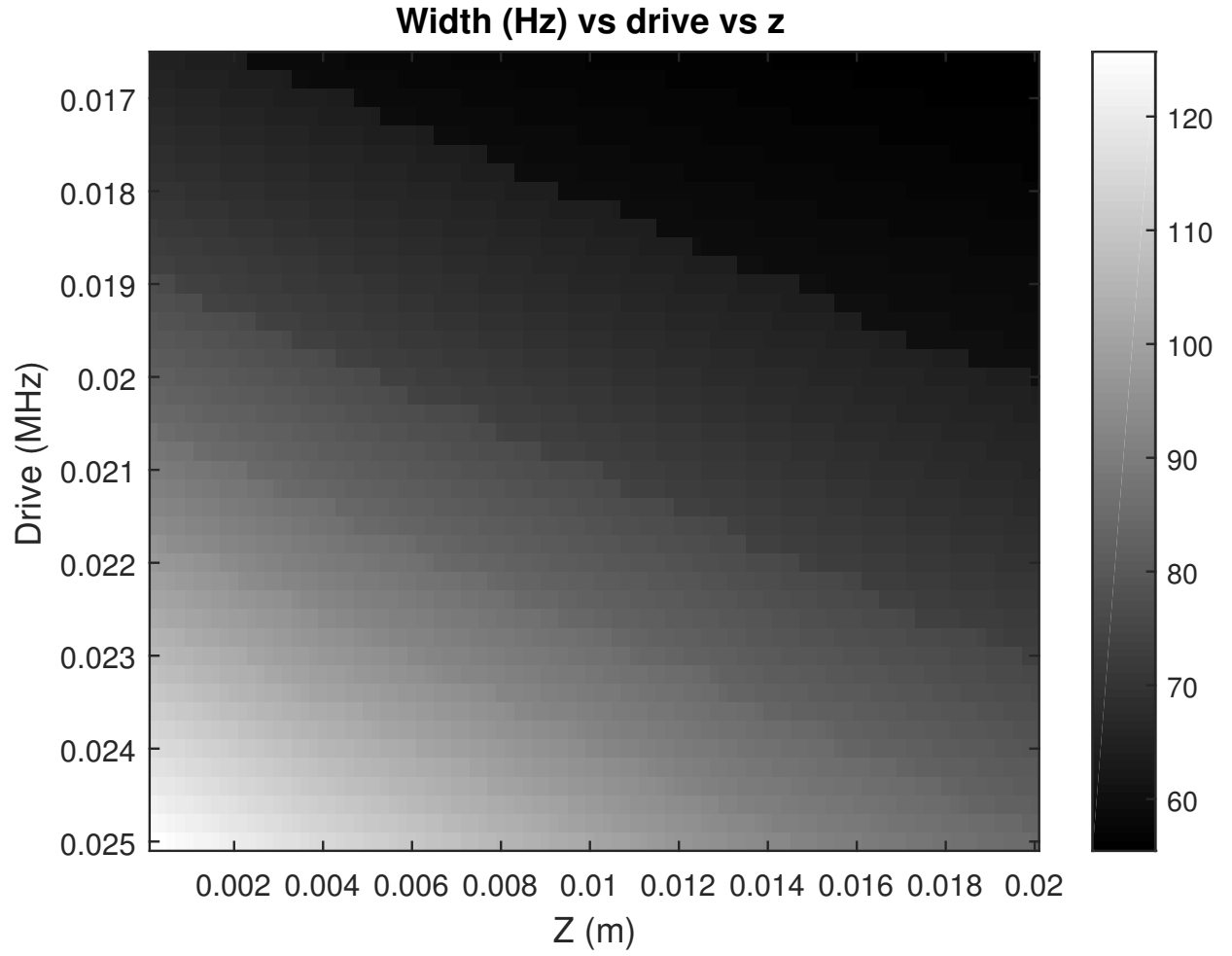


Figure 3.5: This map shows how the linewidth of the EIT is affected by the Drive frequency and length ( $Z$ ) of the atomic media through which the fields are propagating.

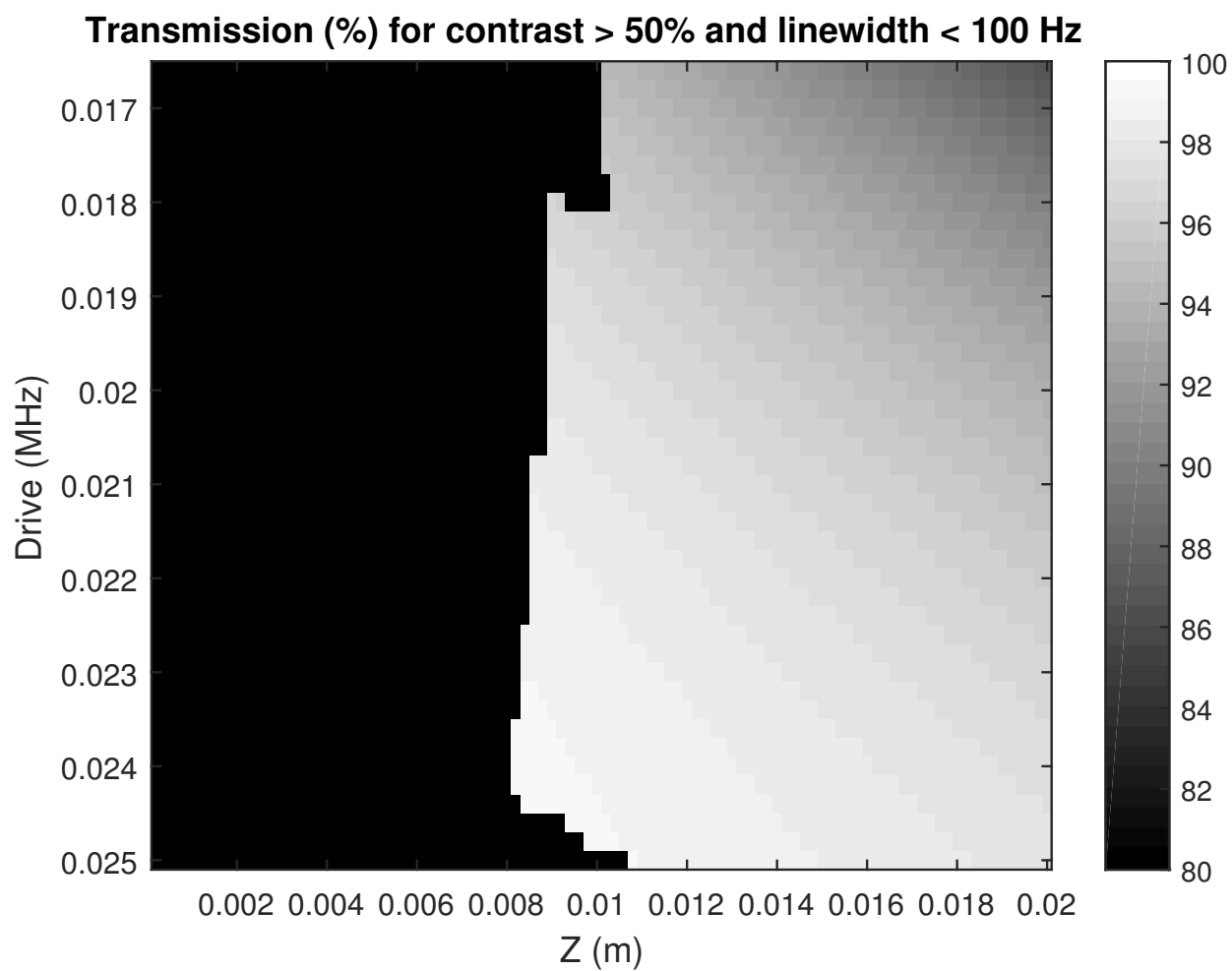


Figure 3.6: This map shows transmission for the regions of drive and  $z$  where contrast is  $> 50\%$  and linewidth  $< 100$  Hz.

# Experiment

## 4.1 Experimental setup and procedures

### 4.1.1 Setup

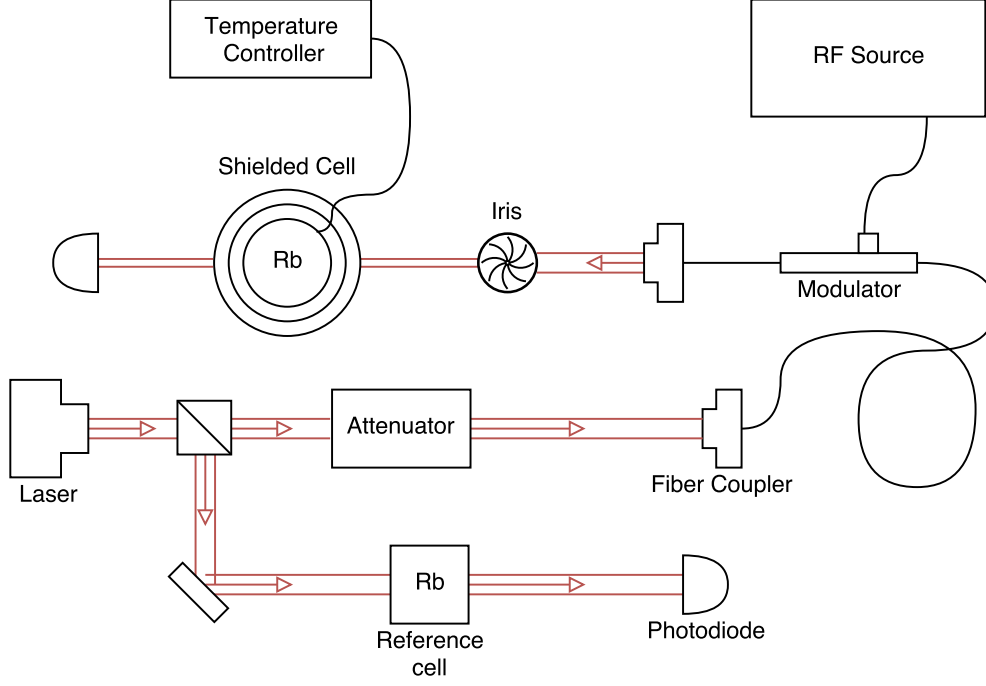


Figure 4.1: A diagram of the experiment configuration.

Figure 4.1 shows a schematic of our experimental setup. We begin with a semiconductor laser tuned to the  $5S_{\frac{1}{2}}, F = 2 \rightarrow 5P_{\frac{1}{2}}, F = 1$  transition frequency of  $^{87}\text{Rb}$  using the reference cell. This is then attenuated before being passed to an electro-optic modulator (EOM). The EOM is provided a frequency of 6.834 GHz, corresponding with the hyperfine splitting of  $^{87}\text{Rb}$ , which is swept through a ramp of 4.768 kHz over a time of 101 ms. This creates a side band with the main beam, to act as our probe and drive fields, respectively. These two fields then pass through a magnetically shielded cell of  $^{87}\text{Rb}$  before reaching a photodiode. The cell is roughly 1.5 cm in diameter and 1 cm in length. It has a high temperature anti-relaxation coating intended to extend the lifetime of the dark state, and so

allow for narrower linewidths. It is temperature controlled using a thermocouple and heating element within the shield, connected to an external temperature controller.

### 4.1.2 Procedures for varying beam intensity

Measurements with varying intensity are done by changing the attenuation of the beam before the cell through the addition of neutral density filters. The resulting power is measured. This measurement is what is used for most of our plots, however this can be converted to a Rabi frequency as reproduced in Equation 4.1 [4].

$$\Omega = 2\pi\gamma\sqrt{\frac{I}{8}} \quad (4.1)$$

Here intensity,  $I$ , is measured in  $\frac{mW}{cm^2}$ . For  $^{87}\text{Rb}$ ,  $\gamma$  is 6 MHz. The power measured is a roughly equal combination of the drive field and two probes (the EOM produces two sidebands at  $\pm$  the modulation frequency). This estimates our drive and probe Rabi frequencies to be in the range of 5 to 30 MHz. This is much larger than the regime which simulations cover, as with our current setup it would not be feasible to detect such small fields.

### 4.1.3 Procedures for varying cell density

Rather than increasing atom-light interactions through lengthening the cell as we did in simulations, experimentally it is easier to increase the density of atoms in the cell. This is done by increasing the temperature. When taking any measurements with varying temperature, we set temperature first, then iterate through any secondary variables such as power. This is due to the prolonged amount of time required for the temperature to become stable at a new point. We have taken measurements for temperatures ranging from 60 to 75 degrees Celsius in increments of 5 degrees. This corresponds to a range in particle concentration of about  $1 \times 10^{11}$  to  $9 \times 10^{11}$  ( $\frac{\text{particles}}{cm^3}$ ) [5].

#### 4.1.4 Procedures for varying beam waist

Although it was not addressed in our simulations, studies with anti-relaxation coated cells have shown that a smaller beam waist results in a finer linewidth of the EIT resonance [6]. In order to incorporate this variable into our study, an iris was placed in front of the Rb cell as shown in Figure 4.1. Rather than attempting sub-millimeter measurements of the beam waist, we quantify the waist size by the percentage of power passed through the iris. These measurements are then converted to a fraction of our beams  $\omega_0$ , the radius at which intensity has dropped by a factor of  $e^2$ . We have taken data for 3 beam waist values:  $3\omega_0$ ,  $1.2\omega_0$ , and  $0.8\omega_0$ , corresponding to roughly 100, 50, and 25 percent of the full beam power, respectively.

## 4.2 Experimental data and data analysis

### 4.2.1 Processing of raw data

As with simulations, we look to measure linewidth and contrast of EIT. In simulation with well shaped absorptive Lorentzian distributions, these were easy to determine with simple analysis. Experimentally, however, the distributions have a dispersive Lorentzian component which makes them asymmetrical. In order to accurately determine the linewidth and contrast, we fit these distributions to a generalized Lorentzian as given in Equation 4.2.

$$Transmission = A \frac{\gamma^2}{\gamma^2 + \delta^2} + B \frac{\gamma\delta}{\gamma^2 + \delta^2} + C \quad (4.2)$$

Here the term with coefficient  $A$  is the absorptive Lorentzian and the  $B$  term is the dispersive Lorentzian. Parameters  $A$ ,  $\gamma$ , and  $\delta$  are the contrast, half width half maximum (HWHM), and 2 photon detuning, respectively [7]. An example of this curve fitted to experimental data is shown in Figure 4.2.

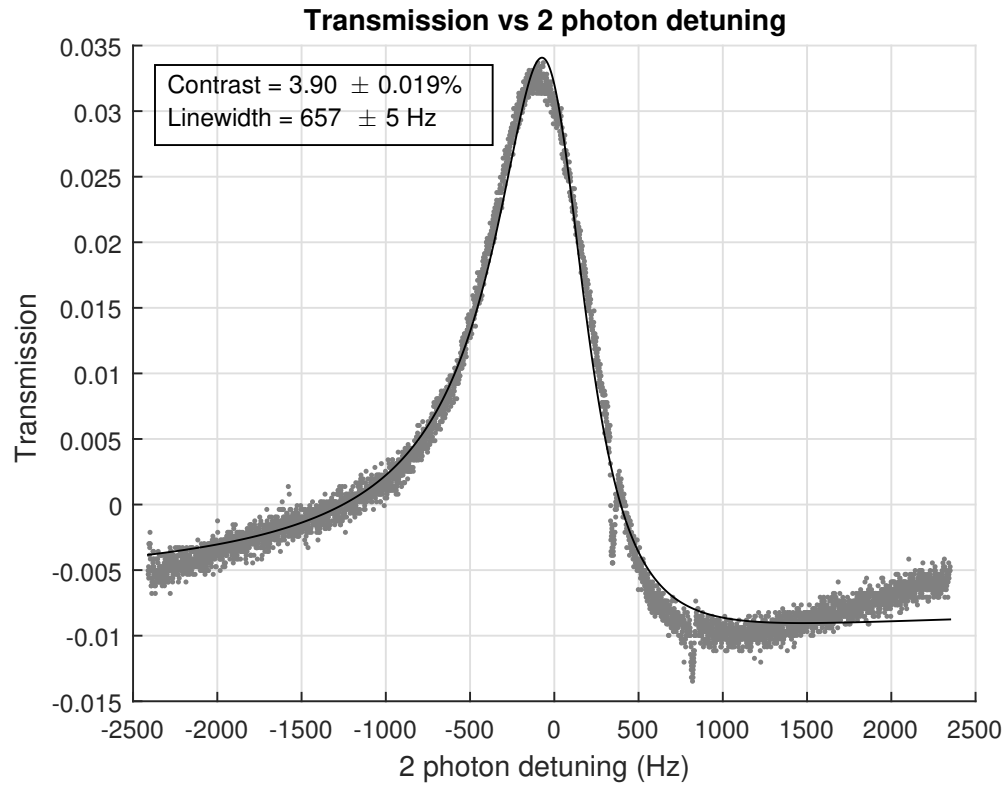


Figure 4.2: Fit of experimental EIT with a contrast of 3.9% and linewidth of 5 Hz. Error bars represent a 95% confidence interval.

### 4.2.2 Contrast and linewidth vs power for varying particle concentration

The data collected as described in Section 4.1.3 is shown in Figures 4.3 and 4.4. These show the contrasts and linewidths, respectively, as functions of drive field power for various rubidium concentrations. We see that contrast increases with drive power before plateauing, as well as a pattern of contrast increasing with density. Both of these results were also observed in simulations (Figure 3.4). Linewidth clearly increases with power, though our smallest linewidth was observed at 260 Hz with a contrast of 0.42%. This experimental trend is expected from the simulation results in Figure 3.5. Unlike our simulation results, however, here linewidth increases with concentration. This is likely due to the ground state decay rate,  $\gamma_{bc}$ , truly being a function of concentration ( $n$ ) and not a constant as it was in simulation. It is clear that we see significantly broader linewidths and smaller contrasts experimentally than in simulation. This is not surprising given that we are operating in a different regime of drive and (especially) probe Rabi frequency.

### 4.2.3 Contrast and linewidth vs intensity for varying beam waist

Figures 4.5 and 4.6 show the data collected as detailed in Section 4.1.4. The x-axis of the plots was converted to a percentage of full intensity from the power measurements in order to show a better comparison of changes in waist size (which have comparable intensities, but different total power). As before, we see that contrast increases with power, both from changes in intensity and changes in waist size. The important observation here is in Figure 4.6, where it is evident that a smaller waist size results in a finer linewidth. The linewidths observed here are roughly a factor of two larger than those seen in Figure 4.4. This is due to error discussed further in Section 4.3. This data contains the largest contrast observed of 3.9% with a linewidth of 660 Hz.

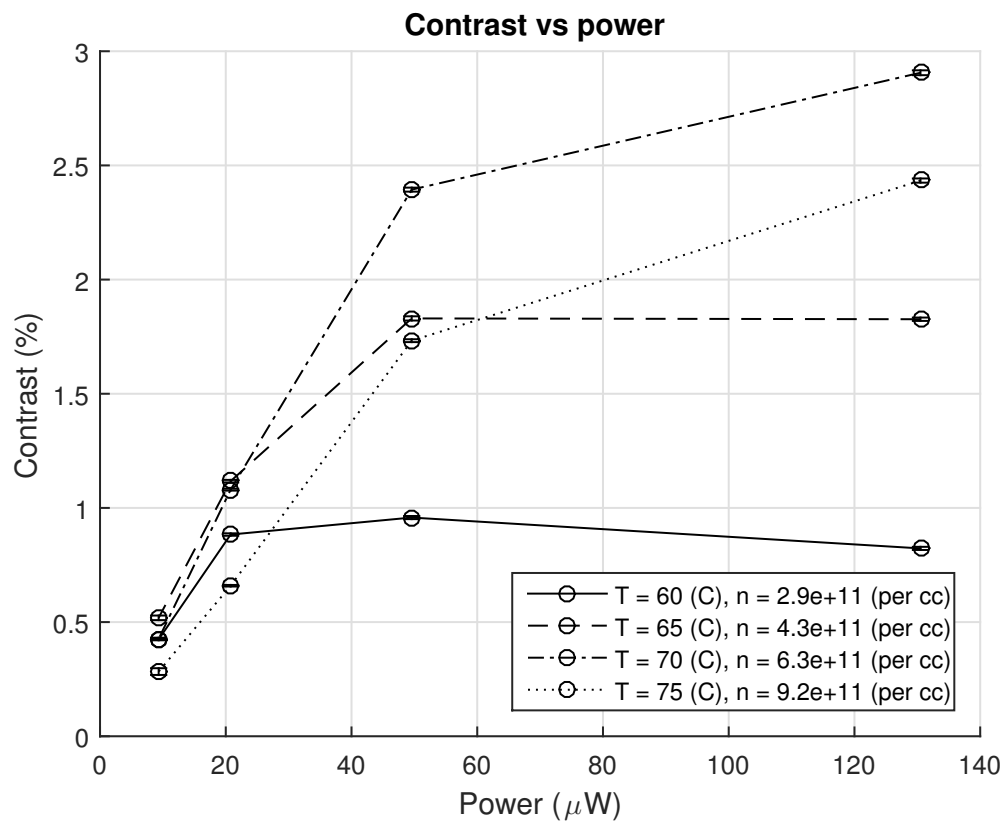


Figure 4.3: Contrast vs power for varying particle concentration

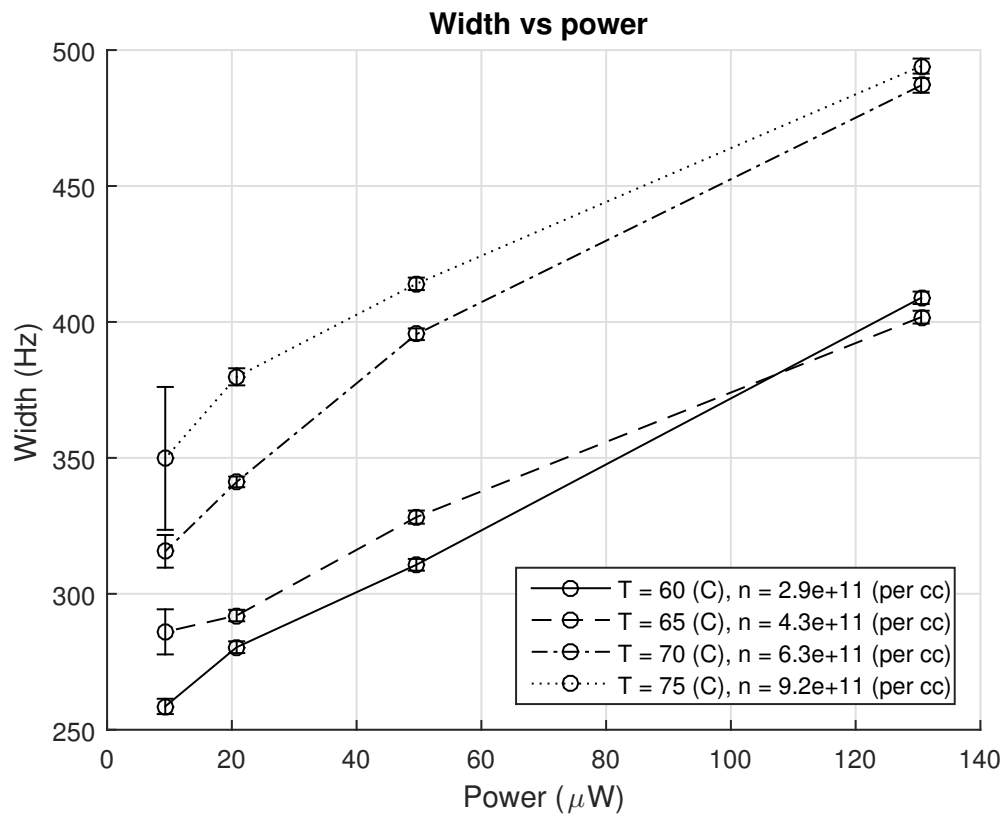


Figure 4.4: Linewidth vs power for varying particle concentration

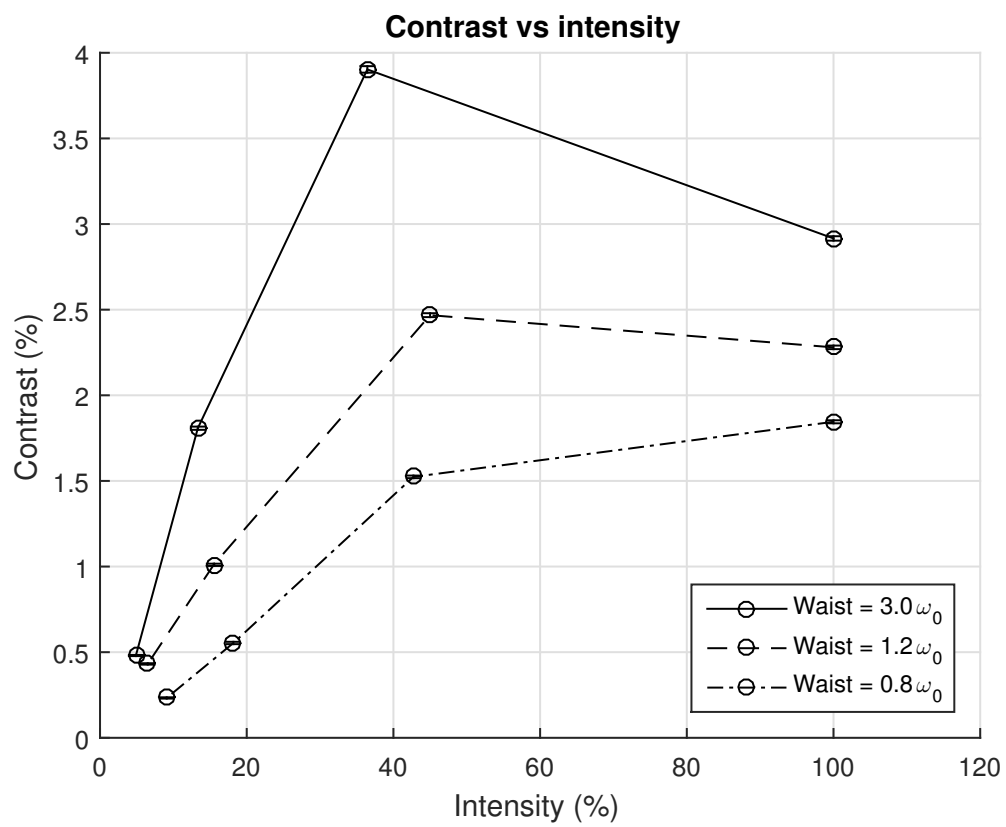


Figure 4.5: Contrast vs intensity for varying beam waist

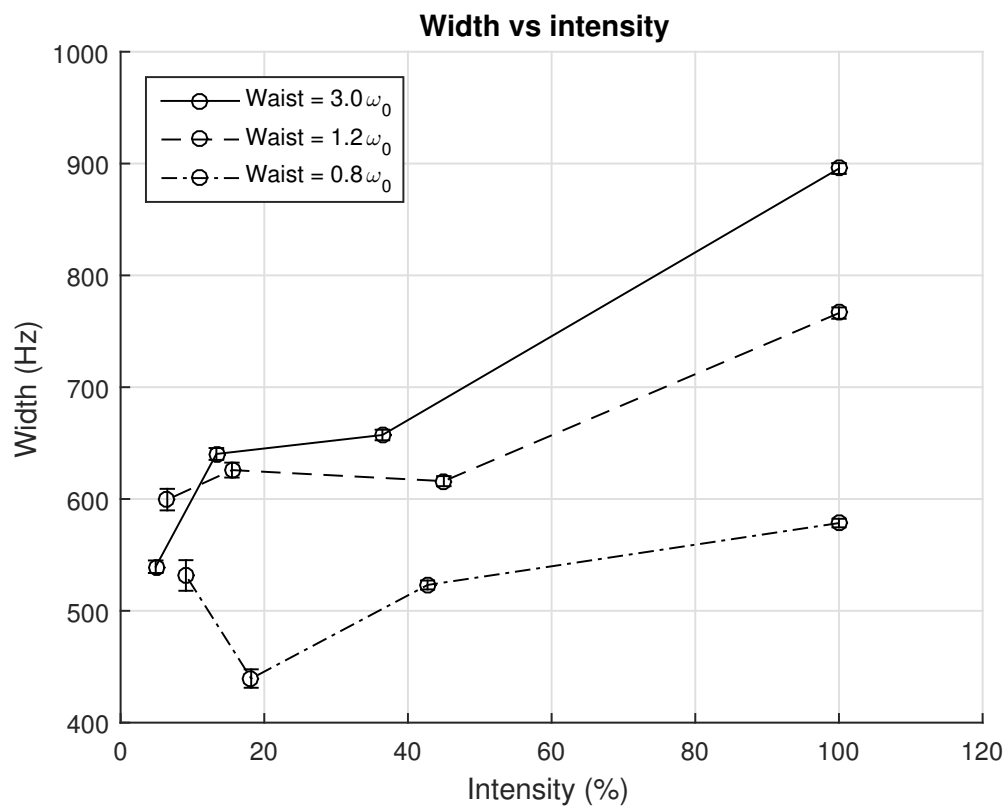


Figure 4.6: Width vs power for varying beam waist

### 4.3 Error analysis

We have encountered multiple noise and error sources which have impacted data collection. These have ranged from benign technical problems involving our heating element, to possibly data altering errors due to faults in electronics. We have identified one of these sources as the magnetic field generated by current between our temperature controller and thermocouple. This has had an affect of widening the resonance linewidths discussed in [Section 4.2](#). We have also observed excessive noise in the data, though the source is not yet known.

# Conclusions

We have simulated EIT in 3 state atoms with properties based on those of  $^{87}\text{Rb}$ . The drive Rabi frequency ranged from 16.6 to 25 kHz with a fixed probe Rabi frequency of 0.1 Hz. EIT with contrasts above 50% and linewidths of less than 100 Hz, suitable for use as a frequency filter, were found in this regime for media lengths of up to 2 cm. We have demonstrated EIT experimentally, though due to technical limitations both our drive and probe Rabi frequencies are several orders of magnitude higher than simulation parameters, ranging from approximately 5 to 30 MHz. Contrast and linewidth are determined by fitting the data to a generalized Lorentzian. The smallest linewidth observed is 260 Hz, with a contrast of 0.42%. The largest contrast observed is 3.9% with a linewidth of 660 Hz.

# References

- [1] H. J. Kimble, Yuri Levin, Andrey B. Matsko, Kip S. Thorne, and Sergey P. Vyatchanin. Conversion of conventional gravitational-wave interferometers into quantum nondemolition interferometers by modifying their input and/or output optics. *Phys. Rev. D*, 65:022002, Dec 2001.
- [2] Eugeny E. Mikhailov, Keisuke Goda, Thomas Corbitt, and Nergis Mavalvala. Frequency-dependent squeeze-amplitude attenuation and squeeze-angle rotation by electromagnetically induced transparency for gravitational-wave interferometers. *Phys. Rev. A*, 73:053810, May 2006.
- [3] Nathan Belcher, Eugeny E. Mikhailov, and Irina Novikova. Atomic clocks and coherent population trapping: Experiments for undergraduate laboratories. *American Journal of Physics*, 77(11):988–998, 2009.
- [4] Eugeny Mikhailov. Nonlinear properties of dense coherent media. 2003.
- [5] Daniel A Steck. Rubidium 87 d line data, 2001.
- [6] M. Klein, M. Hohensee, D. F. Phillips, and R. L. Walsworth. Electromagnetically induced transparency in paraffin-coated vapor cells. *Phys. Rev. A*, 83:013826, Jan 2011.
- [7] S. Knappe, M. Stähler, C. Affolderbach, A.V. Taichenachev, V.I. Yudin, and R. Wynands. Simple parameterization of dark-resonance line shapes. *Applied Physics B*, 76(1):57–63.